

Beamline 10.3.2 at ALS: a hard X-ray microprobe for environmental and materials sciences

Matthew A. Marcus,^{a*} Alastair A. MacDowell,^a
Richard Celestre,^a Alain Manceau,^b Tom Miller,^a
Howard A. Padmore^a and Robert E. Sublett^a

^a*Advanced Light Source, Lawrence Berkeley National Laboratory, 1 Cyclotron Road, Berkeley, CA 94720, USA, and*
^b*Environmental Geochemistry Group, LGIT, University J. Fourier and CNRS, 38041 Grenoble CEDEX, France.*
E-mail: mamarcus@lbl.gov

Beamline 10.3.2 at the ALS is a bend-magnet line designed mostly for work on environmental problems involving heavy-metal speciation and location. It offers a unique combination of X-ray fluorescence mapping, X-ray microspectroscopy and micro-X-ray diffraction. The optics allow the user to trade spot size for flux in a size range of 5–17 μm in an energy range of 3–17 keV. The focusing uses a Kirkpatrick–Baez mirror pair to image a variable-size virtual source onto the sample. Thus, the user can reduce the effective size of the source, thereby reducing the spot size on the sample, at the cost of flux. This decoupling from the actual source also allows for some independence from source motion. The X-ray fluorescence mapping is performed with a continuously scanning stage which avoids the time overhead incurred by step-and-repeat mapping schemes. The special features of this beamline are described, and some scientific results shown.

Keywords: X-ray instrumentation; microspectroscopy; microfluorescence; microdiffraction; powder diffraction; speciation.

1. Introduction

1.1. Scientific objectives

The continuing concern over environmental degradation and contamination has prompted a number of studies of the speciation of toxic elements in soils and plants. The rationale is that the toxicity of an element depends on its bioavailability, which in turn depends on its solubility, which depends on its chemical form. Also, intelligent design of remediation programs requires detailed chemical knowledge of how the toxic elements are sequestered in the environment.

Natural materials such as soils are inhomogeneous over all length scales, down to the nanometer. However, nanometer probes sample extremely tiny sample volumes and often cannot examine dilute species or samples in a natural state. Fortunately, studies have shown that micrometer-scale studies are often sufficient because the nanometer-scale structures are grouped in micrometer-scale aggregates. For example, studies of soil ferromanganese nodules show composition gradients over tens of micrometers which correlate with regions of constant trace-element speciation. Often, these trace elements are sorbed to clays or phyllo-manganates, which are nanostructured materials. Although the nanoscale detail cannot be seen with micrometer-size probes, it can be and has been inferred with a high degree of confidence (Manceau, Marcus & Tamura, 2002).

The field of materials science can also present us with small inhomogeneous samples. Combinatorial libraries are a good example. These samples consist of small patches of different materials, or films

whose compositions vary continuously as a function of position. Other materials examples include defects in semiconductor devices, which may also take the form of small precipitates.

1.2. Specifications of the beamline

The beamline was built to the following specifications:

(i) The source is a 1.27 T ALS bending magnet, whose critical energy is 3 keV.

(ii) The beam is monochromatic, with X-ray absorption near-edge spectroscopy (XANES)-grade resolution and an energy range of 3–17 keV. The lower limit is determined by air absorption; the upper by the decrease in flux with energy of the bending-magnet source and by the wish to reach the U L_3 edge.

(iii) The spot size is 5–17 μm .

(iv) The system must perform X-ray fluorescence (XRF) mapping, followed by XAS and/or X-ray diffraction (XRD) at a point selected with reference to the XRF map.

1.2.1. Characterization techniques and system integration. The three techniques, XRF, XAS and XRD, probe different aspects of the sample, and hence work together to allow a more complete analysis than any one or two of these methods could by themselves. XRF shows where the trace elements are and with which major elements they are associated. Suppose that one finds a pattern in which a trace element, say Ni, is associated with a major one, say Mn. It would be tempting to conclude that Ni is sorbed on or included in a Mn-bearing species, but such a conclusion could be unfounded. The Ni could be in a mineral which grew over a Mn-bearing species, or which was produced by the same chemical processes as the Mn-bearing species but is not a Mn mineral. Therefore, an element-selective probe is needed, which is where XAS comes in. With XAS, one can study the chemical and physical state of small concentrations of the element of interest and ignore the major elements.

Unfortunately, XAS does not provide complete information about the crystal structure of the matrix. In complex materials, XAS can only be interpreted when there is a limited list of possible species. Further, XAS only gives indirect evidence for the crystalline ordering of the host species.

XRD can be used to identify the dominant mineral species at a given location in the sample. While it is not guaranteed that this species is the host of the trace element of interest, the identification of the dominant species can help clarify the sorption behaviour of the trace element. For instance, if XAS shows the trace element incorporated in or sorbed to a mineral which XRD identifies as being a minor constituent, then one might reasonably infer that this mineral may be a stronger sorbent for the trace element than the dominant mineral at the location being probed.

The use of a monochromatic beam for XRF mapping offers some advantages which often offset the disadvantage of having less flux than a white-beam or pink-beam probe (Sparks, 1980). With a white probe, elastic scattering contributes to an intense background over the entire spectrum, whereas a monochromatic probe generates elastic and Compton peaks over a narrow range of energies, which can be tuned to be far away from the line of interest. When the sample is a single crystal or coarse polycrystal, Bragg diffraction can put intense spurious peaks into the spectrum from a white source, whereas such peaks can only be part of the elastic background for a monochromatic source and may often be avoided by changing the energy. Suppose one wants to detect a small amount of an element in the presence of a large amount of another whose edge energy is higher than that of the desired element. In that case, one can place the excitation energy between the two edges and eliminate almost all

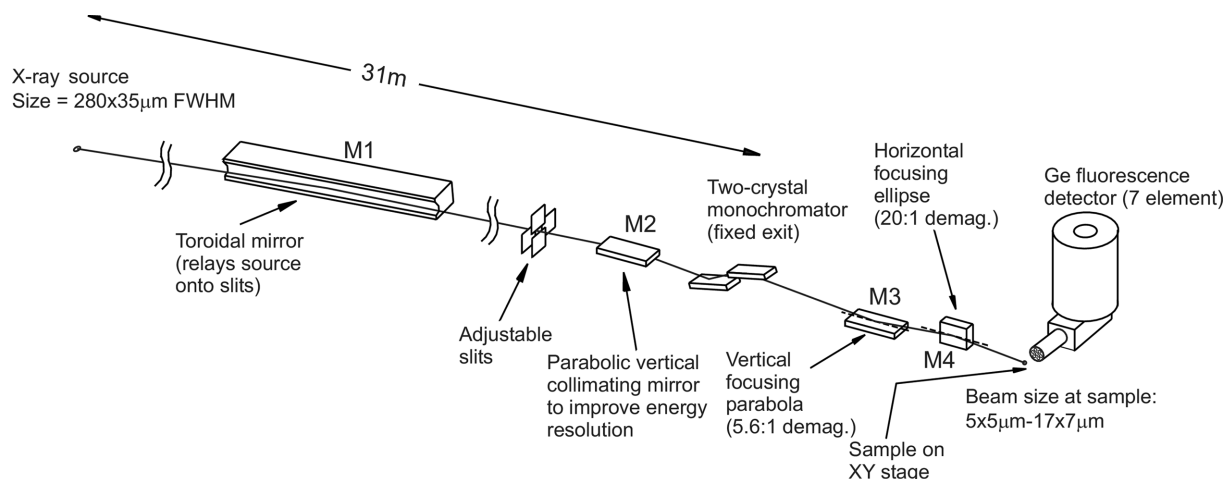


Figure 1
Overall layout of the beamline. Details are as described in the text.

of the background from the unwanted element. Finally, the energy resolution of a solid-state detector such as is usually used for this sort of work is insufficient to distinguish between many common pairs of elements such as Ba/Ti and Pb/As. However, by mapping at energies just above and just below the Pb L_3 edge, one can perform a subtraction to isolate the Pb L_α and As K_α counts separately.

1.3. Role of system integration

To increase the utility and flexibility of the beamline, we have paid particular attention to the integration of the various characterization modes. Multiple computers are used in a network to separate out the low-level beamline control functions from the higher-level data-taking and data-analysis processes.

In general, the sample stage and the fluorescence detector and its electronics are considered to be part of the beamline system, rather than add-ons. Having these items as permanent parts of the beamline minimizes the amount of time lost in the transition between experiments.

2. Optics

The optical layout is as shown schematically in Fig. 1. The source is focused at unit magnification by mirror M1 onto a set of adjustable slits which form a virtual source, which in turn is demagnified by the rest of the optics. The light from this virtual source is collimated in the vertical direction by M2, monochromated by the two-crystal fixed-exit monochromator, then focused to a spot by M3 (vertical focusing) and M4 (horizontal focusing). The demagnification is 20 in the horizontal and 5.6 in the vertical. All mirrors are coated with 8 nm of Rh over 25 nm of Pt over 5 nm of Cr on Si substrates and are used at 4 mrad incidence angle. The rationale for this stack is as follows. The Cr is a glue layer. Platinum is the heaviest reasonable mirror coating so gives the widest energy range for a given angle, but it has L edges at inconvenient energies (11.56, 13.27 and 13.88 keV). Rhodium is not as dense as Pt, but is dense enough to be totally reflecting at 4 mrad incidence angle to energies past the Pt L edges. Thus, an overlayer of Rh hides the Pt in the range over which Pt has edges. Finally, the Pt takes over at energies above where the Rh reflects. M1 is in its own tank with a vacuum in the 10^{-9} torr range, while M2, the monochromator, M3 and M4 are in a tank in the hutch, with a vacuum in the 10^{-7} range. When the slits are fully open, we obtain a source-size-limited image of about $17 \times 7 \mu\text{m}$ ($H \times V$) FWHM (full width at

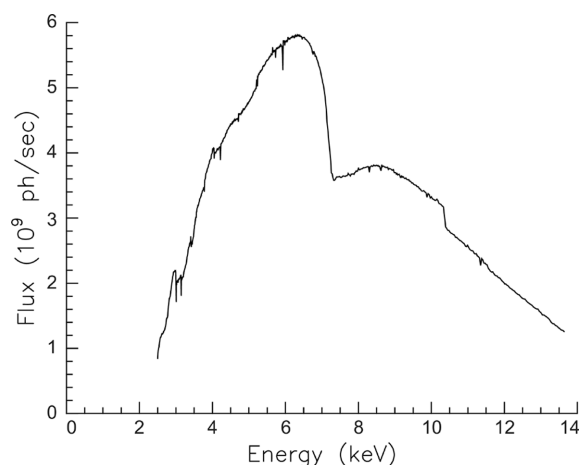


Figure 2
Flux, in photons s^{-1} , of the monochromatic beam at full spot size, plotted as a function of energy. Edges of Cl, Fe, Rh and Pt are visible.

half-maximum). For reasons which are not clear, the minimum spot size appears to be about $5 \times 5 \mu\text{m}$. An effort is underway to acquire new mirrors for M2–M4. The resolution of the monochromator is about 2 eV, depending on the energy. This resolution is sufficient to see the dip at the Cu edge in metallic Cu and the double peak in organobromines. The flux with full beam, as a function of energy, is shown in Fig. 2.

2.1. The virtual source

The virtual source is produced by the first mirror, which is a bent-cylindrical mirror whose short radius is such as to focus in the vertical. This orientation is sideways to the way in which bent-cylinder mirrors are usually used. The reason for this choice is that the source is smaller in the vertical direction than in the horizontal, so we want the vertical to be less influenced by figure errors and roughness than the horizontal. In a normal non-microfocus beamline, this arrangement would be impractical because one would not be able to accept a large amount in the horizontal. However, the focusing mirrors in the hutch can only accept a limited amount of solid angle, so that M1 can be a horizontally deflecting toroid and need only be 0.65 m long. Calculations show that the image of the source, which is about $280 \times 40 \mu\text{m}$ (FWHM), is essentially aberration-free. This image has been used by

the accelerator physicists at ALS as a measure of the beam size in a sector where there is no other means of imaging the beam.

This mirror, to which we refer as M1, is bent by means of torques applied to the ends. Stainless-steel blocks are glued to the end of the mirror, and leaf springs bolted to these blocks. The other end of each leaf spring is bolted to one end of a linear stage, so that the distance between the springs may be varied, thus causing the application of equal couples to each end of the mirror. This design is similar to a vertical deflecting mirror bender used on another hard-X-ray beamline (Hartman *et al.*, 1998). The mirror is not cooled as the absorbed power is calculated to be 0.3 W, leading to an estimated temperature rise of <1 K.

The virtual source size is controlled by a set of roll slits, which consist of pairs of 10 mm rods of polished W in a water-cooled holder. This holder rotates so that, as seen by the beam, the gap between the rods can be adjusted from 0 to 2 mm. There are two such pairs of rods, one for the horizontal and one for the vertical. The cross in which these slits are mounted is separated from the rest of the beamline piping by bellows and is mounted on a translation stage.

Small shifts in the source position can be accommodated by slight rotations of M1 about the vertical or transverse axes. Larger shifts, such as those occurring when the ring is re-surveyed, are accommodated by translations of the roll slits, in addition to rotations of M1. Since the vertical focusing of M1 depends on the incidence angle of the beam, if the source moves a large amount in the horizontal then M1 must tilt and the virtual source also moves. Similarly, the vertical spot size is best if M1 performs no net vertical deflection, so large vertical source motions must be compensated for with both M1 and the slits. However, motions of this magnitude are rare and the normal tune-up is performed just by using M1 rotation in both axes to steer the imaged beam onto the roll slits.

A PIN diode is mounted in a cross just downstream of the roll slits. When M1 tuning is required, the diode is inserted into the beam, the roll slits narrowed and the current on the diode measured.

Machine vacuum is maintained up to just before the roll slits. A water-cooled 50 μm Be window separates the machine vacuum from the hutch vacuum. Thus, testing can be performed with the in-hutch optics in air. Maintenance can be carried out on the focusing optics, monochromator, roll slits and monitor cross without having to bake out the whole beamline to machine-vacuum standards. This window is about 1.1 m upstream of the hutch wall, 0.3 m upstream of the roll slits.

2.2. Focusing and collimating optics

The optics downstream of the virtual source consist of three mirrors (M2–M4) and the monochromator. M2 collimates the beam in the vertical direction so that the monochromator can perform with good resolution. M3 takes the vertically collimated beam from the monochromator and focuses it on the sample, and M4 focuses in the horizontal, making an image of the virtual source on the sample.

All three mirrors are alike, 100 mm long by 12 mm wide by 5 mm thick and made of Si. They are all coated with the same Rh–Pt–Cr stack as M1. All three mirrors in the hutch are mounted in unequal-couple benders with adjustable pitch, translation and end-bending couples as described by MacDowell *et al.* (2001). The bend couples for all three of these mirrors are set off-line using a long-trace profilometer, so the pitch and translation are what are adjusted on-line. M3 and M4 have profiled widths in order to come close to the required shapes upon bending. Picomotors (trademark of New Focus) are used for the motions, with linear variable differential transformers as sensors.

The working distance between the end of the mirror and the focus is about 60 mm. Most of this distance is taken up by the wall of the optics box and a small ion chamber used to monitor the flux incident on the sample (I_0), leaving about 20 mm of air between the ion chamber window and the sample. This distance is small enough so that He bagging is unnecessary for all but the lowest energies.

2.2.1. Beam camera. While tuning up of the mirrors can be performed by means of the traditional knife-edge scan, it is much faster if one has a means of imaging the beam directly. To this end, we built a beam camera which can be inserted into the beam path at the focal plane in place of the sample. This camera consists of a cleaved plate of CdWO₄ followed by a 10 \times microscope objective followed by a low-light monochrome TV camera. The image scale is 0.7 μm per pixel and the resolution is ~ 2 μm , as seen by the sharpness of the images of dust particles when the plate is illuminated with visible light. A video capture program monitors the output of this camera and reports the FWHM in both directions and the position and brightness of the brightest pixel. This program performs frame averaging to reduce noise. It is thus relatively easy to find the optimum angles for the mirrors to produce the sharpest spot.

2.2.2. In-hutch mirrors. The M2 mirror deflects downward and is 1460 mm from the virtual source. Thus, if the source size in the vertical is 40 μm , the vertical divergence, assuming perfect tuning, is 27 μrad , which is comparable with the Darwin width of the Si111 monochromator crystals and contributes 1.3 eV of energy broadening at 10 keV.

M3 deflects upward and focuses from infinity (collimated beam) to the sample, 260 mm away from its center. The net demagnification of the M2–M3 pair is 5.6:1.

A rough optimization of the tilt angle of M2, and thus the vertical collimation of the beam, is performed by taking XANES scans through the white line of Ta foil (L_3 edge), looking for the sharpest highest-possible line. However, this method is not precise enough to come to the correct angle. It is important to have the vertical collimator tuned correctly because M2 and M3 are coupled. It is possible to obtain a sharp focus with M2 overfocusing and M3 underfocusing or *vice versa*. Thus, we need a method of judging when M2 is collimating. When the mirrors are tuned up correctly, a sharp image of the virtual source is formed at the sample and the monochromatic beam between the mirrors is collimated. Now, it is possible to shift the beam vertically by translating the second crystal of the monochromator so as to change the gap between the crystals. If M3 truly images from infinity, the image on the sample will not move when the beam is shifted vertically with respect to M3. Thus, the setting of M3 can be checked by moving the monochromator crystal and looking at the image on the beam camera. Another way to test the tuning is to move the roll slits by known amounts and measure the displacement of the beam. The tuning is only correct when the demagnification is 5.6:1. This latter method is not as precise as the monochromator-shift method. A final check of the resolution can be made by scanning the organobromine XANES feature in a commercial plastic such as Lexan or Plexiglas. These materials include organobromines in sufficient quantity to yield a strong Br signal.

The horizontal-focus mirror M4 is bent into an elliptical shape and deflects in the same direction as M1. It has a demagnification of 20:1 and a centre-image distance of 119 mm. It is tuned up by closing down the roll slits and adjusting the tilt for best image. Small adjustments of one of the bend couples are sometimes also necessary to obtain the smallest spot size.

The power absorbed by the mirrors is quite small, so cooling in the usual sense is unnecessary. However, it is desirable to stabilize the temperature of the mirrors and their mounts. The mirror mounts are

attached to a rail to which is attached a chill block through which temperature-controlled water passes. Since the mirrors are in a vacuum, there is little thermal contact between them and the outside except for this mounting rail, so this simple system should isolate the mirrors from temperature variations in the hutch.

An illustration of the spot quality is shown in Fig. 3, which is a fluorescence map of a thin patterned Ta film in which a cross of 40 μm line-width has been etched from the centre. This test object was made according to the method of David *et al.* (2000). The curves on the top and right-hand sides of the map are line-outs of the intensity. The curve does not go to zero in the vertical direction because there is significant scatter by the mirrors. We have replaced M2 since these data were taken and now see much less scatter. The resolution is about 5 μm FWHM in each direction.

2.3. Monochromator

The height and width of the incident beam are determined by the desire to fill the mirrors. Thus, the monochromator must take a beam of about 400 $\mu\text{m} \times 400 \mu\text{m}$. It must be reasonably agile, in case quick-EXAFS experiments are required in the future. The energy resolution has to be good enough to perform XANES, and the energy range must cover edges from S to U L_3 (6–60° Bragg angle for Si111). It must be stable enough to run unattended overnight without retuning. The output beam must be fixed in height and especially in angle. Since the vertical-focusing mirror M3 is optically like a lens distant from the sample by an amount equal to its focal length, an angular deviation from the monochromator transforms to a position shift of the beam on the sample. This monochromator is designed with a 3 mm fixed offset. Because it handles a small beam with a small offset, its mechanics are quite different from the usual front-end monochromator such as one might find on a general-purpose X-ray beamline.

The monochromator is a two-crystal design using Si111 crystals. The crystals are mounted on a common shaft which provides the rotation. In addition, the second crystal translates to keep the exit beam at a constant height. The position of the first crystal is carefully chosen relative to the centre of rotation of the shaft so that the beam

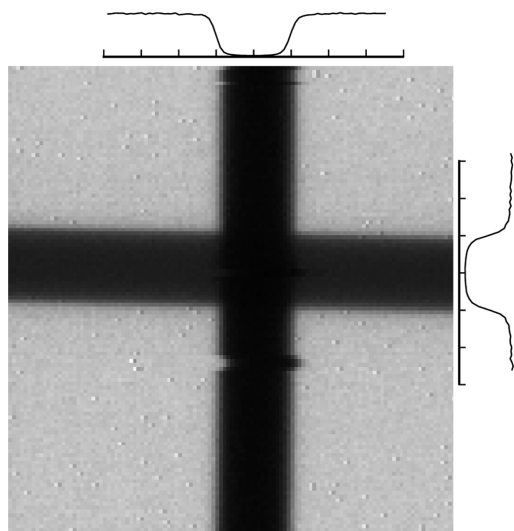


Figure 3
Map of a Ta-film test object in which a cross pattern has been etched out. The lines of the cross are 40 μm wide. The curves above and to the right of the image are line profiles showing the resolution. The ticks on the axes are 20 μm apart.

‘walks’ as little as possible on both crystals. The geometry of the monochromator is shown in Fig. 4. The 0° configuration is shown only for reference. The monochromator is shown accepting a 1 mm-high beam. Since the beam is actually 0.4 mm high, this design has some margin.

The crystals are simple rectangular blocks 10 mm \times 10 mm \times 20 mm in size. This small size makes them easy to mount and to cool, and is a result of the small beam size. The 10 mm \times 20 mm reflecting face on each crystal is polished.

A servo-motor-driven Huber goniometer with a 180000 counts rev^{-1} Heidenhain rotary encoder drives and supports the main shaft. All cooling and wiring passes through this shaft to prevent wire drag on the mechanism as shown in Fig. 5. The main shaft is sealed with a differentially pumped rotary seal system of LBNL design. Crystal 1 is water cooled and rigidly mounted. This crystal is glued with silver-filled epoxy to a copper submount which is in turn attached with screws to a copper chill block. Thermal contact between the submount and chill block is assured by a 0.05 mm-thick

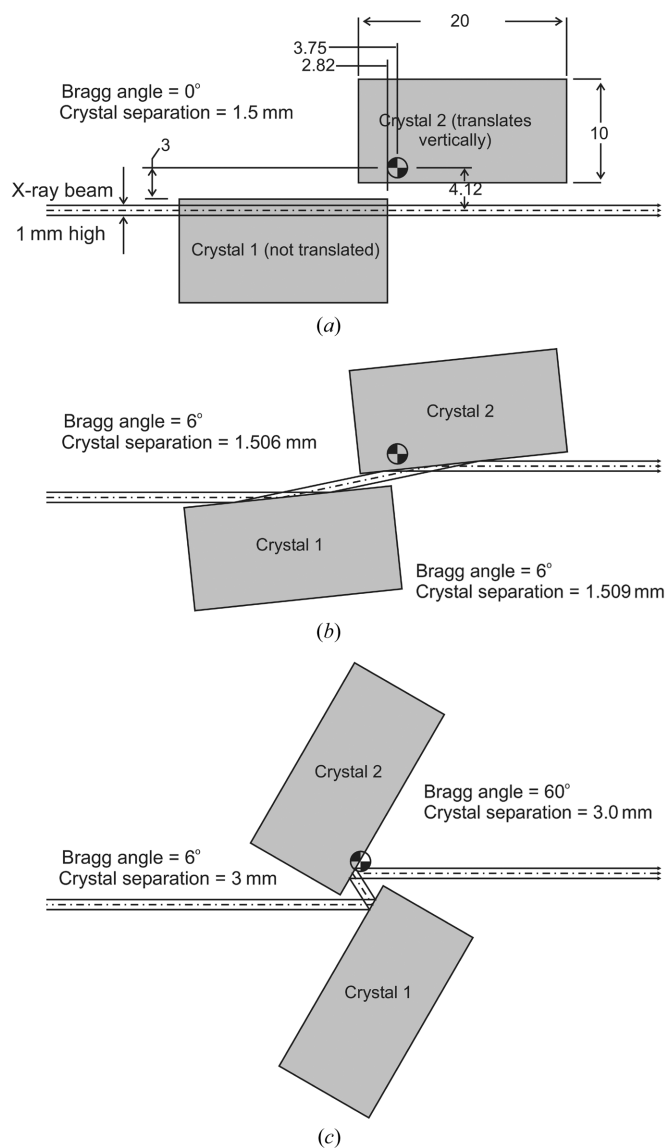


Figure 4
Geometry of the monochromator, showing Bragg angles of 0° (reference only), 6° and 60°. A 1 mm-high beam is shown incident from the left. All dimensions shown are in millimeters.

InGaSn eutectic layer. All copper parts that are in contact with the eutectic are nickel plated to prevent alloying. Water to the chill block is fed through the support structure for crystal 1. The joints are O-ring sealed. There are no air guards or dedicated water lines in this mechanism. Actually, the absorbed power is small enough to make cooling unnecessary; the real function of the cooling system is temperature stabilization. Crystal 2 is glued with silver-filled epoxy to an aluminium submount. This submount is screwed to a 1.5 mm travel LBNL-designed flexural stage. This stage is centered with the crystal spacing at 2.25 mm. A picomotor drives against a spring to set the spacing. The spring pushes against an LVDT (linear variable differential transformer) core, which pushes on a wobble pin that operates the flexure. The flexure position is thus measured by the LVDT. The flexure is mounted on a notch hinge assembly. This hinge controls the pitch (Bragg angle) adjustment of crystal 2. The hinge is spring loaded and driven by a picomotor with LVDT feedback. The axis of rotation for this hinge is the main shaft axis. This geometry minimizes the amount by which the crystal translates as the pitch is adjusted. This pitch mechanism mounts on an equivalent hinge mechanism for roll control. Any correction of roll on crystal 2 will result in a translation of the crystal in the same axis as the flexure. This has not been an issue, as the pitch and translation adjustments do not result in roll errors. The submount of crystal 2 is thermally anchored to the same cooled support structure as that for crystal 1, so both crystals are temperature-stabilized.

The completed mechanism was bench aligned with a height gage and an indicator. All flexures were set to their null points with crystal 2 in proper relation to crystal 1 for a mid-range energy. The mechanically complete mechanism is shown in Figs. 5 and 6.

3. Monitoring

We have already described two forms of monitoring, the PIN diode after the roll slits and the beam microscope for tuning the mirrors.

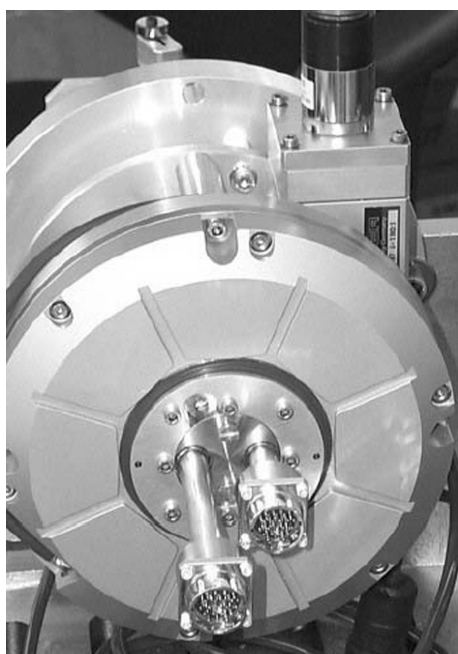


Figure 5
View from the air side of the monochromator, showing the encoder (large annular object with radial grooves), the motor/gear reducer combination and the mounting flange. The picomotor which adjusts the crystal translation is visible at the top.

However, for XAS, good normalization can only be achieved if the incident beam is monitored after all the optics. Thus, a short-path ion chamber was built on the end of the optics box. A 50 μm -thick Be window separates the optics box from the ion chamber. The path length of the ion chamber is about 20 mm. At most energies, N_2 is a satisfactory fill gas, though a He/ N_2 mixture must be used at the lowest energies, and Ar at the highest. The end of the ion chamber has a 6 μm -thick aluminized-Mylar window.

4. Detection

Fluorescence is detected by a Canberra seven-element Ge detector (Ultra LEGe, 50 mm^2 per element) running into XIA electronics (DXP2X Model T). These modules take the place of shaping amplifiers and multichannel analysers (MCAs). There are two modes of operation, single point and mapping. In single-point mode, a pulse-height (MCA) spectrum is collected from each detector element. Counting is enabled by a gate signal from a timer board, such that counts accumulate only when the gate signal is high. The output counts are read back under software control. The single-point mode is used for XAS data collection as well as for inspection of the MCA spectrum at any desired location.

The other mode is mapping. In this mode the DXP modules are pre-set with up to 16 spectral bins (regions of interest, ROIs) and access an internal memory which can be thought of as a two-dimensional array with as many rows as there are bins set. Upon receipt of a gate pulse, counts are accumulated into the ROIs. When the next gate pulse comes in, the counts are loaded into a column of the two-dimensional array and the ROIs cleared so counting can begin again. An address pointer is incremented so that the next set of counts are written into the next column of the data array. A start command initializes the system and a stop command ends data acquisition. Thus, when the stop command has been issued, the

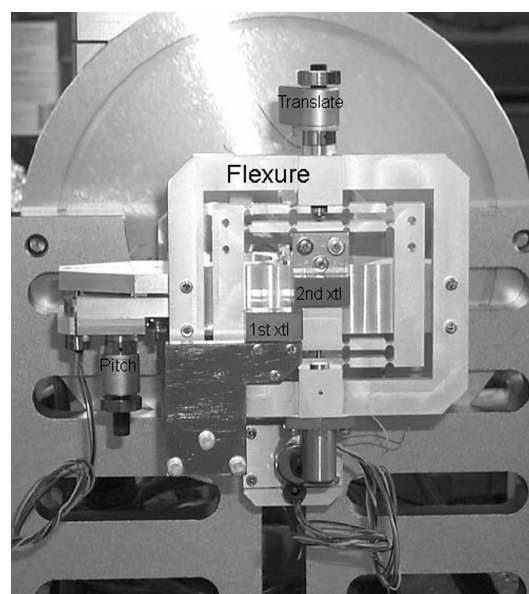


Figure 6
View of the monochromator from the vacuum side. The beam enters from the left as in Fig. 4. The monochromator is set for 0° Bragg angle, as in Fig. 4(a). The translation motor is visible at the top, and the pitch motor at the left. The gray blocks are the crystals, and the square aluminium assembly surrounding them is the flexure device which moves the second crystal without tilting it. The monochromator is shown mounted on a temporary scaffold rather than on the beamline, which is why the O-ring groove is visible at the top.

internal memory contains a summary of the spectra of X-rays detected during each of a number of gate pulses. The driver for the horizontal translation stage can be configured to emit the appropriate gate pulses at user-settable intervals. The result is that a line scan can be accumulated during a continuous move of the stage and read out when the stage reaches the end of the line. By repeating this action, with a motion of the vertical stage in between each line, we accumulate a two-dimensional map of the sample in up to 16 'colours' or spectral bins. The energy calibration in this mode is the same as in single-point mode, so single-point MCA spectra may be used for guidance in setting the bins. This method of mapping is much more efficient than the traditional step-and-repeat mode, in which the stage dwells on each point for a given time, and thus must start and stop at each point.

In principle, it would have been possible to use histogramming memory to build a system in which the entire spectrum was stored at each point. However, this would have increased the required data-transfer rate 128-fold and made the task of displaying the data much more complex for both programmer and user. Also, no commercial system like XIA's exists with this functionality. Further, the large size of the data files produced by such a system would have meant that a binary format would be required for storage, with all the inconvenience and lack of portability that entails. For all these reasons, we opted for the reduced flexibility of a system which allows the collection of only 16 bins per sampling point. For most of what is performed on this beamline, this mode provides sufficient flexibility.

The off-the-shelf version of the XIA software requires a TCP/IP server to be running, which mediates between commands from the host program and the DXP modules. We found that the overhead involved with TCP/IP calls was prohibitive, so the vendor provided a custom version of their software which could be called directly from *LabVIEW* (National Instruments).

The detector elements run with a peaking time of 1 μs , which translates into a measured dead time of 3.2 μs per element. This choice represents a compromise between detector speed and resolution, which is 250–300 eV FWHM for Mn K_{α} . It is possible to perform a dead-time correction accurately enough for XAS at count rates of up to about 300 kHz per seven elements. A typical situation is that a sample will produce a few kHz of counts from Zn, in which we are interested, but hundreds of kHz of Fe counts. In that case, one to five sheets of aluminium foil make an effective filter. If the total count rate is still too high after filtering, the detector can be translated away from the sample on a linear slide.

5. Diffraction

Diffraction data are collected using a Bruker SMART6000 CCD detector mounted on a three-axis (XZ Θ) stage. The detector may be moved out of the way when not needed and quickly re-positioned. The stage allows one to change the sample–detector distance to capture different ranges of d spacings. Lattice spacings down to 1 \AA may be collected by raising the incident energy to 15 keV. A clear pattern may be collected from a 0.5 μm Fe foil in 1 s at this energy. At the other end of the spectrum, rings have been seen with d spacings of up to 40 \AA . The usual exposure time is 1 min at 14 keV, which provides a clear signal on poorly crystallized or nanophase materials.

The detector software is not at present integrated with any of the other programs on the beamline.

6. Examples of scientific results

In this section we summarize three examples of scientific research which have been performed on this beamline. Two of these are related to environmental issues, as this area is the one for which the beamline was intended, while the third is an example of materials science.

6.1. Speciation of Ni in a soil

This work was published by Manceau, Tamura *et al.* (2002), so will be described only in broad outlines.

Soils often contain ferromanganese nodules, which are millimeter-size sub-round concretions rich in nanocrystalline Fe and Mn oxides. These nodules are thought to be the result of fluctuating redox chemistry, which results in the deposition of layers of Fe and Mn. These oxides have very large surface areas, so can sorb large quantities of trace minerals. It is commonly found that trace elements are enriched in these nodules relative to the surrounding soil.

In this work the environment of Ni was investigated by means of XRF, XAS and XRD. The XRD was performed at another beamline, 7.3.3, which has a unique diffraction mapping capability not yet available on 10.3.2, but XAS was performed at 10.3.2. XRF mapping was undertaken at both beamlines in order to establish a correspondence between points probed by XRD and XAS. The samples consisted of thin sections of nodules fixed in resin, so the nodules were seen in cross section.

It was found that the distribution of Ni, seen by XRF, matched that of lithiophorite, as seen by XRD mapping. These distributions, for one nodule, are shown in Fig. 7. This mineral is a layered compound consisting of alternating MnO_2 and $\text{Al}(\text{OH})_3$ layers, with alkali or alkali earth ions between the layers. The obvious inference is that Ni is sorbed to this mineral, being included in the structure or attached to the layers or the layer edges. However, it cannot be assumed that an association between an element and a mineral implies that the element is incorporated in that mineral. For example, the Ni could be part of a phase which was deposited on or formed under the same conditions as lithiophorite.

EXAFS was performed at the Ni K edge, at a number of locations on the nodules. The EXAFS patterns were everywhere the same, and were different from that of synthetic Ni-sorbed lithiophorite. Analysis of the EXAFS and comparison with Mn-edge EXAFS showed that the Ni was indeed incorporated into the lithiophorite structure, but substituting in the Mn layers. The laboratory reference had Ni in the Al layers instead. Representative EXAFS patterns for the sample and reference are shown in Fig. 8.

This example shows the usefulness of applying the three techniques, XRF, XAS and XRD, together on one sample. While 10.3.2 cannot yet carry out XRD mapping, it can perform powder patterns at single points of interest.

6.2. Forms of Zn accumulation in a plant

Our next example is also from the published literature, from Sarret *et al.* (2002). It concerns the storage of Zn in a hyperaccumulating plant, *Aribidopsis halleri*. High levels of Zn are toxic to most plants. If soil is contaminated with Zn, a very common pollutant, then plants will not grow well in it unless some treatment is applied to reduce the bioavailability of the Zn. One of the many ways being tried is phytostabilization, in which plants which can grow at high Zn concentrations pick up the metal and store it in a form which is insoluble, hence less harmful to other organisms than the original form.

It was known that *A. halleri* could store large amounts of Zn, but what was not known was where the Zn was put and in what form. X-ray diffraction revealed nothing because the Zn was not in a well crystallized form. XRF mapping showed Zn in the leaves, roots and especially the trichomes (hairs) on the leaves. Such a map is shown in Fig. 9, along with EXAFS spectra from specific areas of the plant. It was found that there was a uniform background of Zn in the leaves and roots, but the trichomes showed enhanced Zn concentrations, especially in small collars around their bases. The EXAFS spectra showed that the Zn was stored in different forms, depending on where it was in the plant.

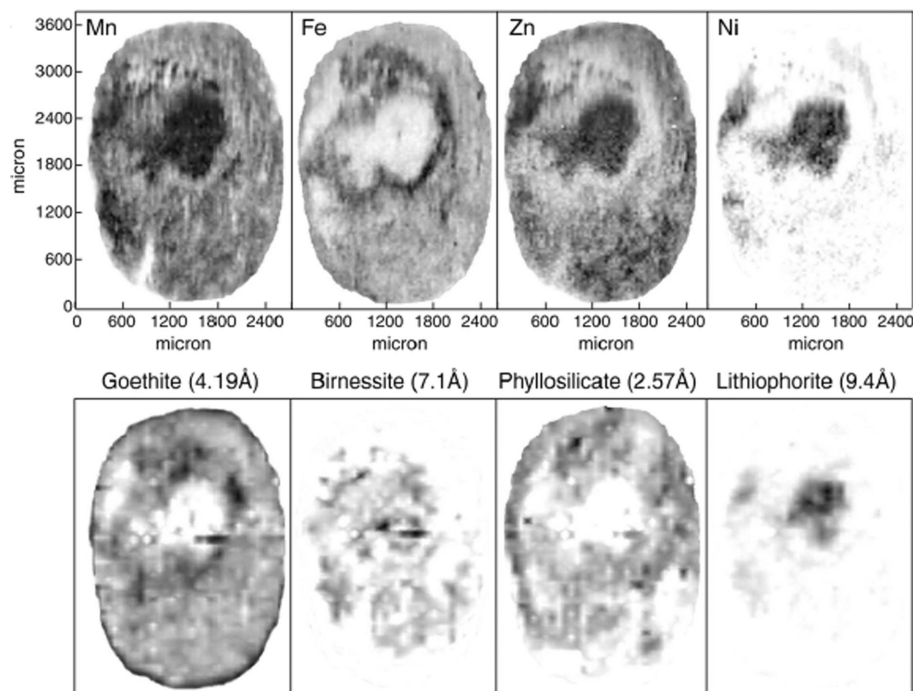


Figure 7
Distributions of Ni, Zn, Mn and Fe in a soil nodule are shown in the upper row. The corresponding distributions of goethite, birnessite, phyllosilicate and lithiophorite are shown in the bottom row. All distributions are plotted in negative-contrast grayscale so that high concentrations are shown as dark areas. We see that the distribution of Ni matches that of lithiophorite and does not match those of the other minerals.

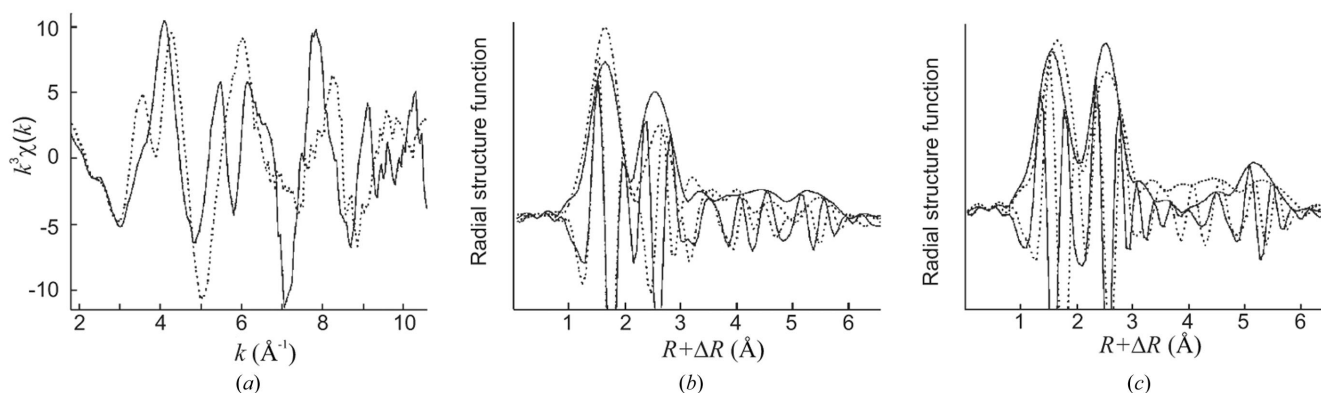


Figure 8
EXAFS patterns for Ni in the soil nodule for which the elemental and mineralogical distributions are plotted in Fig. 11, and for the synthetic reference. (a) Ni-edge EXAFS (full line: soil lithiophorite; dotted line: reference), (b) its Fourier transform (full line: soil lithiophorite; dotted line: reference) and (c) the Fourier transform of the Ni-edge (dotted line) and Mn-edge (full line) EXAFS of soil lithiophorite. [Taken from Manceau, Tamura *et al.* (2002).]

6.3. Structural anisotropy of oriented nanoclusters

This work-in-progress, carried out in collaboration with D. Michiko Aruguete, Liang-shi Li, and A. P. Alivisatos, involves using polarized EXAFS to look at the structural anisotropy of CdSe nanorods. These rods form a nematic liquid crystal which is oriented over small (<100 μm) domains (Li *et al.*, 2002). Thus, a microbeam is required to probe an area which is homogeneously oriented. We have performed Se *K*-edge EXAFS with the rods oriented at various angles to the polarization of the beam. In order to find a domain oriented as desired, we record diffraction patterns, an example of which is shown in Fig. 10. The sharp arc is the basal (002) reflection of the wurzite structure. That it is an arc instead of a continuous ring demonstrates the orientational ordering. The other arcs are fuzzy because their diffraction wavevectors are not along the long axis, so there are a limited number of diffracting planes in those directions.

EXAFS data taken in several different orientations are shown in Fig. 11. In order to accentuate the difference between the two orientations, we have subtracted the oscillations corresponding to the first shell, leaving the second and higher shells. We see that there is an effect of orientation, whose magnitude agrees roughly with a simple model of the rod as being bounded by a cylindrical surface without faceting. Thus, this preliminary result demonstrates that we can use polarized EXAFS, in combination with spontaneous orientational ordering, to probe the surface structure of these particles.

7. Future developments

We intend to implement scanning XRD, which will allow for mineral mapping as in Manceau, Tamura *et al.* (2002). Also, we are considering a plan to move the beamline from its present bending-magnet source to one of the new 5 T superbends (critical energy = 12 keV) which have recently

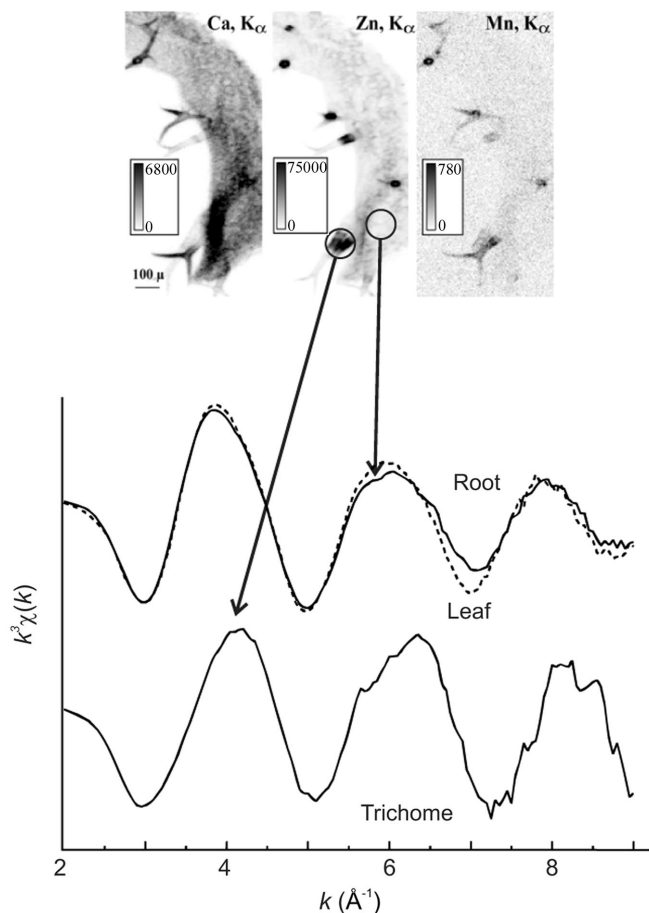


Figure 9
Upper panel: XRF maps of Ca, Mn and Zn in leaves of *A. halleri* plants showing concentrations of Zn in ‘collars’ around the trichome bases and Ca in the tips. Lower panel: the Zn micro-EXAFS spectra from a trichome, the body of a leaf, and a root.

become available at the ALS (Robin *et al.*, 2002; Tamura & Robinson, 2002). This new source will provide more flux in the 8–20 keV range allowing useful experiments on dilute samples of the important contaminants U and Pb.

8. Summary and conclusions

Beamline 10.3.2 is a facility in which three microscale techniques, μ XRF, μ XAS and μ XRD, are brought together in a way which is optimized for certain kinds of environmental research. Although the beamline was designed with a particular type of experiment in mind, it is versatile enough to be used for many other experiments not originally anticipated. A unique combination of X-ray optical hardware, detectors, software and system integration makes it possible to carry out experiments which can be performed in few other places.

The Advanced Light Source is supported by the Director, Office of Science, Office of Basic Energy Sciences, Materials Sciences Division, of the US Department of Energy under Contract No. DE-AC03-76SF00098 at Lawrence Berkeley National Laboratory. The Ta-film test object was loaned to us by Christian David and Daniel Grolmund of the Paul Scherrer Institute.

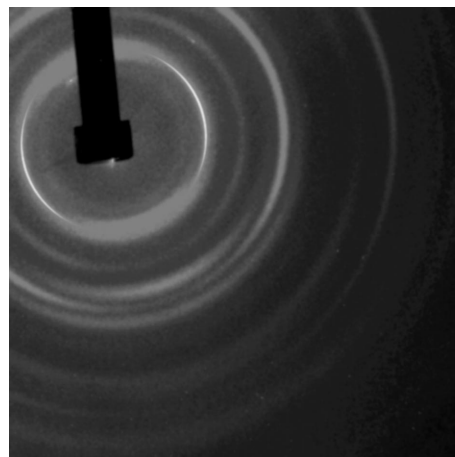


Figure 10
Diffraction from oriented nanorods of wurzite-structure CdSe. The sharp intense reflection is the (002) reflection, which shows the effect of orientational ordering. The dark shape is a beamstop.

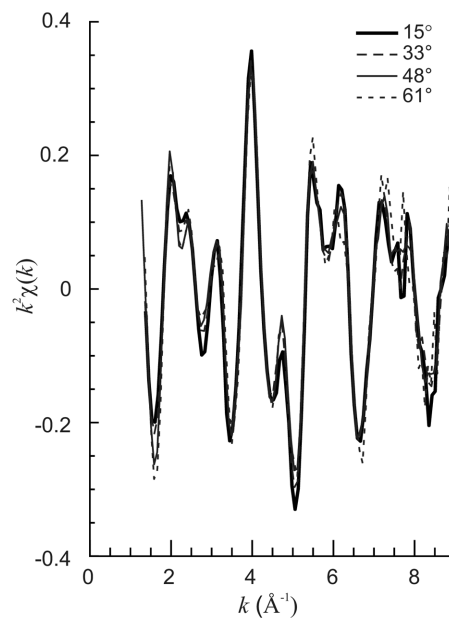


Figure 11
Se *K*-edge EXAFS from CdSe nanorods oriented at several angles to the polarization. The first shell (Se–Cd) has been subtracted from each spectrum to highlight the higher shells. The angles are 15° (thick line), 33° (long dashes), 48° (thin line) and 61° (short dashes).

References

David, C., Musil, C., Souvorov, A. & Kaulich, B. (2000). *Proceedings of the Sixth International Conference on X-ray Microscopy*, edited by W. Meyer-Ilse, T. Warwick and D. Attwood. New York: American Institute of Physics.
Hartman, N. D., Heimann, P. A., MacDowell, A. A., Franck, K. D., Grieshop, A. P., Irick, S. C. & Padmore, H. A. (1998). *Proc. SPIE*, **3447**, 40–51.
Li, L. S., Walda, J., Manna, L. & Alivisatos, A. P. (2002). *Nanoletters*, **2**, 557–560.
MacDowell, A. A., Celestre, R. S., Tamura, N., Spolenak, R., Valek, B., Brown, W. L., Bravman, J. C., Padmore, H. A., Batterman, B. W. & Patel, J. P. (2001). *Nucl. Instrum. Methods*, **A467/468**, 936–943.
Manceau, A., Marcus, M. A. & Tamura, N. (2002). *Rev. Mineral. Geochem.* **49**, 341–428.

- Manceau, A., Tamura, N., Marcus, M. A., MacDowell, A. A., Celestre, R. S., Sublett, R. E., Sposito, G. & Padmore, H. A. (2002). *Am. Mineral.* **87**, 1494–1499.
- Robin, D., Benjegerdes, R., Biocca, A., Bish, P., Brown, W., Calais, D., Chin, M., Corradi, C., Coulomb, D., De Vries, J., DeMarco, R., Fahmie, M., Geyer, A., Harkins, J., Henderson, T., Hinkson, J., Hoyer, E., Hull, D., Jacobson, S., Krupnick, J., Marks, S., McDonald, J., Mollinari, P., Mueller, R., Nadolski, L., Nishimura, K., Ottens, F., Paterson, J.A., Pipersky, P., Ritchie, A., Rossi, S., Salvant, B., Schlueter, R., Schwartz, A., Spring, J., Steier, C., Taylor, C., Thur, W., Timossi, C., Wandesforde, J. & Zbasnik, J. (2002). *Proceedings of the 8th European Particle Accelerator Conference*, Paris, pp. 215–217.
- Sarret, G., Saumitou-Laprade, P., Bert, V., Proux, O., Hazemann, J. L., Traverse, A., Marcus, M. A. & Manceau, A. (2002). *Plant Physiol.* **130**, 1815–1826.
- Sparks, C. J. (1980). In *Synchrotron Radiation Research*, edited by H. Winick and S. Doniach. New York: Plenum Press.
- Tamura, L. & Robinson, A. (2002). *Synchrotron Rad. News*, **15**, 30–34.